ACS APPLIED MATERIALS & INTERFACES

Research Article

www.acsami.org

Influences of Porous Structurization and Pt Addition on the Improvement of Photocatalytic Performance of WO_3 Particles

Osi Arutanti,[†] Asep Bayu Dani Nandiyanto,[‡] Takashi Ogi,*[,†] Tae Oh Kim,[§] and Kikuo Okuyama[†]

[†]Department of Chemical Engineering, Graduate School of Engineering, Hiroshima University, 1-4-1 Kagamiyama, Higashi Hiroshima 739-8527, Japan

[‡]Departmen Kimia, Fakultas Pendidikan Matematika dan Ilmu Pengetahuan Alam, Universitas Pendidikan Indonesia, Jl. Dr. Setiabudhi No. 229 Bandung 40154, Indonesia

[§]Department of Environmental Engineering, Kumoh National Institute of Technology, Daehak-ro 61, Gumi, Gyeongbuk 730-701, Korea

Supporting Information

ABSTRACT: Tungsten trioxide (WO_3) displays excellent performance in solar-related material applications. However, this material is rare and expensive. Therefore, developing efficient materials using smaller amounts of WO_3 is inevitable. In this study, we investigated how to create high photocatalytic performance of WO_3 particles containing platinum (Pt, as a co-catalyst) and homogeneously spherical macropores (as a medium to enable access of large molecules and light penetration into the remote internal regions of the catalyst). The present particles were prepared by spray drying of a precursor solution containing WO_3 nanoparticles, Pt solution, and polystyrene (PS) spheres (as a colloidal template). Photocatalytic studies showed that changes in particle morphology (from dense with smooth surfaces, to dense with rough surfaces, to porous structures) and added Pt effectively improved the photocatalytic performance over WO_3 nanoparticles. Our results showed that the best precursor (prepared using a PS/WO_3 mass ratio of 0.32 and containing Pt co-catalyst) provided WO_3 particles with a photocatalytic rate of more than 5 times that of pure 10 nm WO_3 nanoparticles. Moreover, the catalyst can be effectively recycled without an apparent decrease in its photocatalytic activity. The experimental results were also supported by a proposal mechanism of the photocatalytic reaction phenomenon.

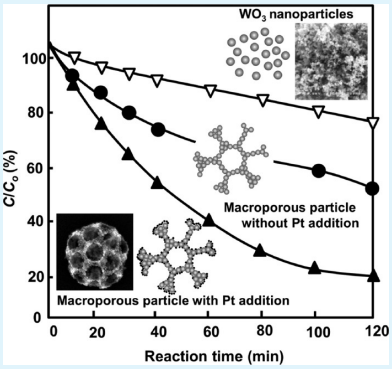

KEYWORDS: *macroporous structure, self-organization, nanoparticle, submicron, surface activation, visible light irradiation*

1. INTRODUCTION

Tungsten trioxide (WO_3) is an excellent prospective material for a wide range of applications (e.g., electrocatalysts, sensors, photochromic devices, and photocatalysts) due to its attributes: relative harmlessness, chemical and thermal stability, good photostability, and chemical and biological inertness.[1−8] However, the use of WO_3 is limited by its disadvantages: expense and rarity.[9] Further, although WO_3 is active under visible light, pure WO_3 material has a low efficiency.

Extensive efforts have been devoted to improve the performance of WO_3 as a catalyst. We briefly described the previous research to provide context for the novel approach that will be presented in this study regarding the morphology control and Pt addition as a co-catalyst. Huang et al.[10] and de Respinis et al.[1] reported the synthesis of mesoporous WO_3 materials. Although the presence of mesoporous structure enhances the photocatalytic performance, some limitations associated with mesoporous structures remain. Mesoporous structures can easily collapse during long heat treatments. Furthermore, the presence of a small pore size regime entails difficulties associated with mass transfer and diffusivity, and the transport of molecules either in or out of the pore system. To maximize the number of active components, Ashkarran et al.[11] and Martínez-de La Cruz et al.[12] reported the synthesis of nanometer-sized WO_3 particles. The use of nanoparticles is effective to maximize the number of WO_3 active components and improve photocatalytic performance. However, the downstream processes employed for the reuse or removal of the nanoparticles is typically expensive, and direct disposal of nanoparticles poses several environmental problems. Incorporation of Pt metal as co-catalyst was also reported as another alternative way to improve the catalytic activity of WO_3.[9,13−19] However, current methods require specific and complex synthetic equipment with rigorous conditions. Furthermore, most of the reports describe the synthesis of WO_3 materials from tungsten salt. The use of tungsten salt typically leads to the formation of a compact and dense material that features inactive components in the inner regions of the catalyst. These inner components cannot interact with the target molecule and light for molecule photodegradation.

Received: June 14, 2014
Accepted: January 21, 2015
Published: January 21, 2015

DOI: 10.1021/am507935j
ACS Appl. Mater. Interfaces 2015, 7, 3009−3017

In our previous studies, we also successfully synthesized WO_3 particles using a spray-pyrolysis method. We focused on morphological control (i.e., particle size and shape),[20] crystal structure optimization,[21] and co-catalyst incorporation.[22,23] However, we were not concerned on with further optimization of the photocatalytic performance. Specifically, we used tungsten salt as a WO_3 particles source.[24]

Herein, we report the synthesis of spherical macroporous Pt-modified WO_3 particles via a spray-drying method. Different from our previous reports, here, we used WO_3 nanoparticles as a WO_3 source that is expected to produce larger surface areas. The internal morphology of WO_3 particles was controlled using polystyrene (PS) sphere as the sacrificial colloidal templates in the initial precursor. The current method also affords control of the porous structure in the particle by varying the PS-to-WO_3 mass ratios, which most reported papers have not examined. This method has potential for generating efficient materials but using relatively low amounts of raw materials.

The photocatalytic studies showed that changes in the morphology and incorporation of Pt as a co-catalyst were effective to improve the photocatalytic performance over WO_3 nanoparticles. The experimental results were also supported by a proposal mechanism of the photocatalytic reaction phenomenon. In addition, owing to the size of the prepared particles that is within the submicron range, the particles have prospects in industry-related applications because they can be collected easily from the waste solution and reusable.

2. EXPERIMENTAL METHOD

2.1. Preparation of Spherical Macroporous Pt-Modified WO_3 particles. Spherical macroporous WO_3 particles were prepared from a precursor solution containing WO_3 nanoparticles (Nisshin Engineering Inc., Japan; a mean size of 10 nm) and 250 nm polystyrene spheres (PS; synthesized from styrene monomer (Kanto Chemical Co., Japan) and 2,2′-azobis (isobutyramidine) dihydrochloride (Sigma−Aldrich, USA)). Detailed information on the synthesis of the PS spheres is provided in our previous study.[25] To tailor the porous structure of the particle, we varied the PS/WO_3 mass ratio from 0.00 to 0.40. To prepare WO_3 with added Pt co-catalyst, hydrogen hexachloroplatinate (IV) hexahydrate ($H_2PtCl_6{\cdot}6H_2O$; Sigma−Aldrich, US) was added to the precursor. In addition, prior to add PS into the precursor, 0.40 wt % of polydiallyldimethylammonium chloride (PDADMAC; Sigma−Aldrich, US) was added. The composition of the precursor solutions used in this study is shown in Table 1.

The precursor was then introduced into the spray-drying apparatus schematically depicted in Figure 1. Detailed information about spray-drying apparatus and mechanism is reported in elsewhere.[26] Briefly, the apparatus consisted of an ultrasonic nebulizer (NE-U12; Omron Corp., Japan; operating at a frequency of 1.7 MHz), a ceramic tubular furnace (diameter of 30 mm and length of 1.3 m) with two temperature-controlled zones set at 200 and 600 °C, and a filter. To introduce the droplet generated by the ultrasonic nebulizer into the tubular furnace, air at a flow rate of 0.5 L/min was used. Additionally, we prepared spherical dense WO_3 particles using ammonium tungstate pentahydrate (ATP; Kanto Chemical Co., Japan) as a dense particle with a smooth surface as other comparison.

2.2. Characterization. To examine the morphology of the prepared particles, a scanning electron microscope (SEM; S-5000; Hitachi Co., Japan; operating at 20 kV) and a transmission electron microscope (TEM; JEM-3000 F; JEOL Co., Ltd., Japan; operating at 300 kV) were used. The crystallinity and phase structure of the prepared particles were examined using an X-ray diffraction (XRD; Rigaku Denki RINT2000, Japan; using Cu Kα radiation and a 2θ scanning range of 20−80°). Thermal analysis of the samples was conducted on a thermal gravity and differential thermal analyzer (TG−DTA; Exstar6000; Seiko Instruments, Inc., Japan; using a heating rate of 5 °C/min and carrier gas (air) at a rate of 200 mL/min). Elemental mapping and chemical composition of the prepared particles were evaluated using a scanning transmission electron microscope (STEM) equipped with energy dispersive X-ray spectroscopy (EDS). Surface area was analyzed by using Brunauer−Emmett−Teller measurement (BET; BELSORP 28SA, Bel, Japan, nitrogen adsorption isotherms at 77.15 K).

The photocatalytic activity of the prepared particles was assessed by mixing 0.20 g of the prepared particles with 1.00 mg of rhodamine B (RhB; Wako Pure Chemical Industries Ltd., Japan) in 500 mL of aqueous solution. The mixed solution was introduced into the batch reactor equipped with a solar simulator system (PECL11, Peccell Technologies, Inc., Japan; AM 1.5G (100 mW/cm^2)). To maintain the concentration of dissolved oxygen during the photocatalytic process, 200 mL/min of oxygen was bubbled into the reactor. To measure the concentration of RhB in the reactor, 3 mL of the mixed solution was

Table 1. Composition of Raw Materials Used in the Precursors

sample	WO_3 source	UPW (mL)[a]	PS (mL)[b]	Pt source (mL)[c]
dense particle	ATP (6.3 g)	100		
aggregated particles	WO_3 nanoparticles (4.00 g)	100		
aggregated particles with macropores	WO_3 nanoparticles (4.00 g)	100	24[d]	
	WO_3 nanoparticles (4.00 g)	100	32[e]	
	WO_3 nanoparticles (4.00 g)	100	40[f]	
aggregated particles with Pt	WO_3 nanoparticles (4.00 g)	100		1.20
aggregated particles with macropores and Pt	WO_3 nanoparticles (4.00 g)	100	32[e]	1.20

[a]UPW = ultra pure water. [b]We used 2.00 wt % of PS in water. Prior to adding PS into the solution, we added 0.40 wt % of PDADMAC. [c]Prior to using, we diluted Pt source ($H_2PtCl_6.6H_2O$) into UPW with a concentration of 0.05 g/mL; [d]PS/WO_3 mass ratio = 0.24.; [e]PS/WO_3 mass ratio = 0.32. [f]PS/WO_3 mass ratio = 0.40.

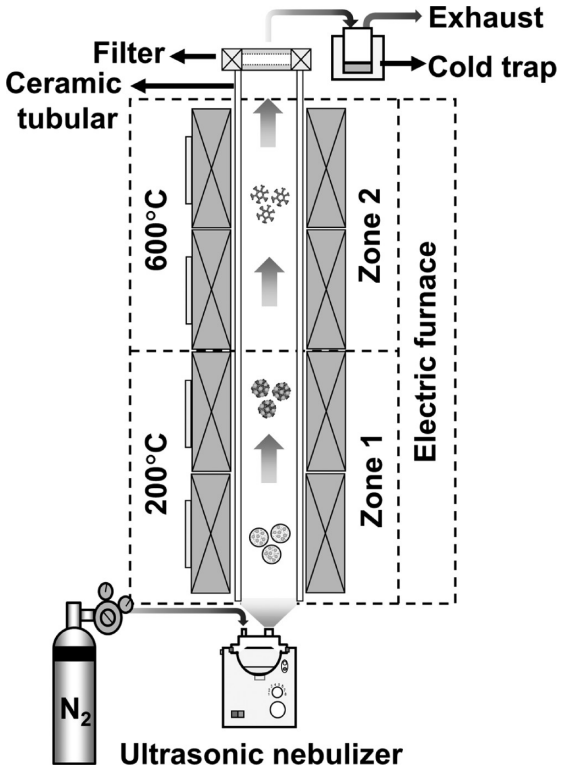

Figure 1. Schematic illustration of the spray-drying apparatus.

DOI: 10.1021/am507935j
ACS Appl. Mater. Interfaces 2015, 7, 3009−3017

sampled every several minutes. Prior to analysis, the sampled solution was then centrifuged at 15,000 rpm for 5 min. The concentration of RhB in the sample was measured using a UV−Vis spectrophotometer (UV-3150; Shimadzu Corp., Japan).

3. RESULTS AND DISCUSSION

3.1. Physicochemical Properties of Raw Material. Figure 2 shows electron microscopy images of the raw materials used in this study (i.e., WO_3 nanoparticles and PS spheres). SEM images in Figure 2a,b showed that relatively monodisperse particles were obtained. The sizes of WO_3 and PS spheres were around 10 and 250 nm, respectively. TEM images in Figure 2c,d showed that all particles were dense. These results confirm that these colloidal materials can be used for preparing particles with homogeneous structures.

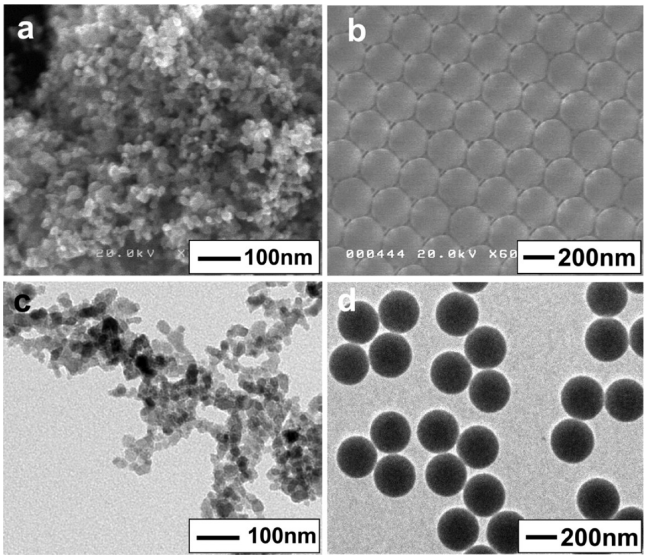

Figure 2. Typical (a and b) SEM and (c and d) TEM images of the raw materials used in this study: (a and c) WO_3 nanoparticles and (b and d) PS spheres.

To ensure the formation of porous structures within the particles, TG−DTA analysis was conducted (Figure 3). The three types of samples analyzed were PS only, WO_3 nanoparticles only, and PS/WO_3 (prepared at a PS/WO_3 mass ratio of 1.00). As observed, WO_3 sample displayed minimal mass losses with increasing heating temperatures. In contrast, samples containing PS (i.e., PS only and PS/WO_3 samples) exhibited a significant mass loss from 270 °C. Then, the mass was relatively stable after passing temperatures of 400 °C. The final masses of the PS only and PS/WO_3 samples were 0 and 48%, respectively. Because the amount of WO_3 added to the PS/WO_3 sample coincided with the final mass after the drying process, it can be concluded that the PS component was completely removed, generating pure WO_3 as the final product.

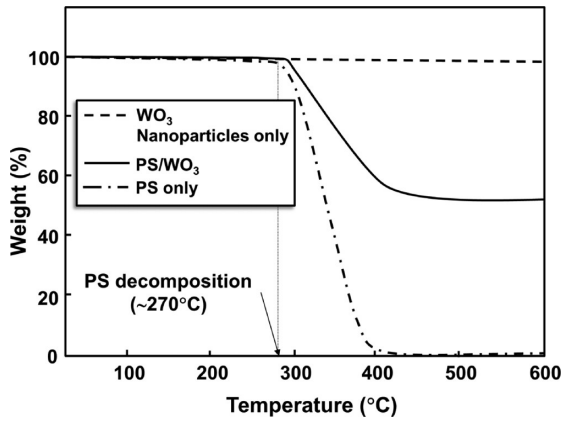

Figure 3. TG−DTA analysis of WO_3 nanoparticles only, PS/WO_3, and PS only samples.

3.2. Preparation of Spherical Macroporous Pt-Modified WO_3 Particles. Figure 4 shows electron microscopy images of particles prepared with varying PS/WO_3 mass ratios. For comparison, we also analyzed WO_3 particles prepared from ATP solution (Figure 4a).

The use of precursor containing WO_3 source only resulted in particles without a macroporous structure (Figure 4a,b). When using the precursor containing ATP as the WO_3 source, the process produced spherical particles with a smooth surface and a mean size of about 0.6 μm (Figure 4a). The use of precursor containing WO_3 nanoparticles without PS addition generated particles with rough surface with a mean size of about 0.6 μm (Figure 4b). These results indicate that surface area of the prepared particles with a rough surface is higher than the particles with a smooth surface.

Figure 4c−e depicts SEM images of the spray-dried particles prepared with varying PS/WO_3 mass ratios. The addition of PS to the precursor allowed the preparation of particles with macroporous structures, whereby the number of macropores in the particle increased with increasing PS amounts. However, further increases in the PS amount resulted in fractured particles. The mean sizes of particles (shown in Figure 4 c−e) were 0.8, 0.8, and 0.7 μm by increasing mass ratio of PS/WO_3 of 0.24, 0.32, and 0.40, respectively.

From the above results, the optimum ratio required for the production of highly ordered macroporous structures is 0.32 (Figure 4d). Deviation from the optimum mass ratio led to a disordered macropore arrangement. Insufficient mass ratios resulted in fewer macropores. In contrast, excessive mass ratios (excess content of PS in the precursor) inhibited disruption of the macroporous structure of the final particle (Figure 4e).

To further evaluate the macroporous structure of the particle, we conducted TEM analysis (Figure 4f,g). As shown in Figure 4f, the skeleton structure was due to the self-assembly of the WO_3 nanoparticles and resulted in the produce of small cavities. Furthermore, Pt metal was detected on the particle surface. The red circles in Figure 4f indicate the existence of agglomerate Pt on the particle surface. The mean size of Pt was of 1.9 nm. HRTEM image in Figure 4g exhibits the crystalline structure of WO_3 and Pt with the lattice spacing was of 3.8 and 2.29 Å, respectively.

The structure and crystallite sizes of the prepared particles were identified by XRD patterns, as depicted in Figure 5. The XRD patterns show that the all prepared particles were consistent with the standard JCPDS No. 72-1465. This number was indexed to monoclinic structure of WO_3 with orientation 002, 020, and 200. The all crystallite sizes were determined to be ~6 nm from the broadening peal area by using the Scherrer method. The phase and pattern of the nanoparticles and spray-dried particles were similar, suggesting that spray drying did not induce a change in the WO_3 crystallinity of the particle. Also, Pt peaks were not detected, likely because the content of Pt is lower than the detection limit of the XRD technique.

To confirm the existence Pt in the prepared particles, STEM, elemental mapping was conducted (Figure 6). STEM analysis

DOI: 10.1021/am507935j
ACS Appl. Mater. Interfaces 2015, 7, 3009−3017

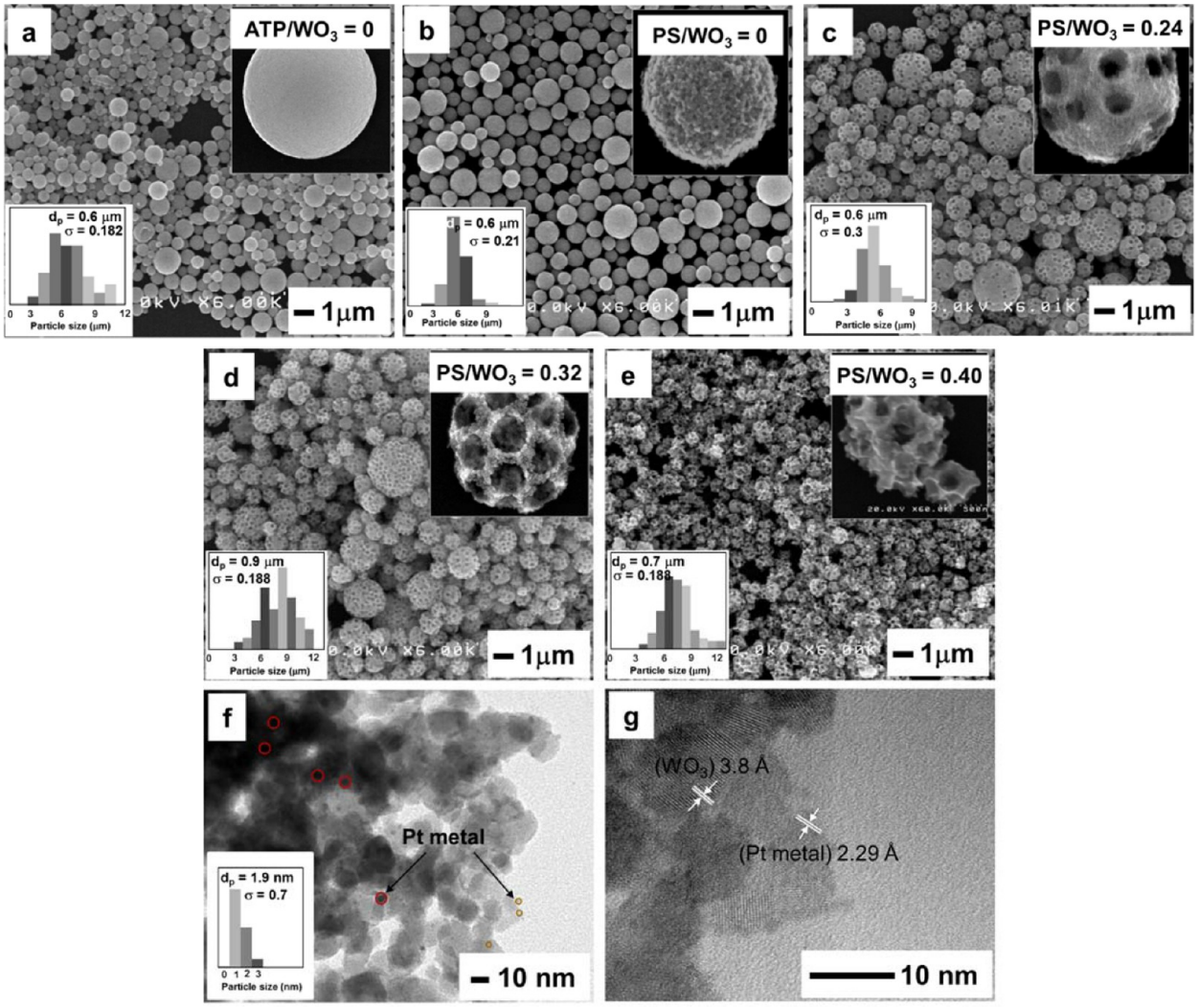

Figure 4. SEM images of the spray-dried particles: (a) prepared from ATP and (b–e) prepared using varying PS/WO_3 mass ratios of 0.00, 0.24, 0.32, and 0.40, respectively. (f and g) High-resolution TEM images of macroporous particles with the PS/WO_3 mass ratio of about 0.32.

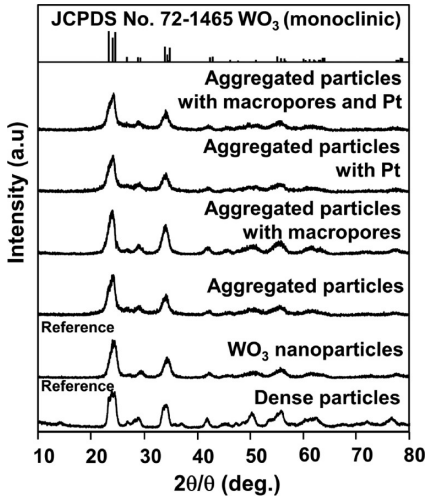

Figure 5. XRD patterns of the as-prepared particles using varying compositions of PS and Pt addition in the precursor.

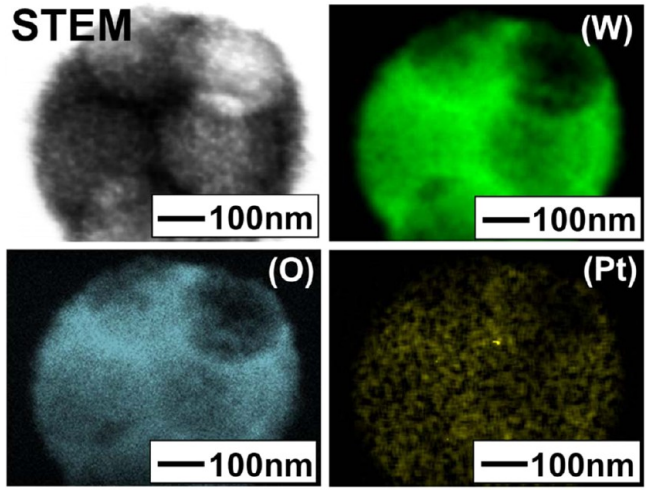

Figure 6. STEM image of prepared particle and corresponding elemental mapping images showing the presence of W, O, and Pt elements in the sample.

revealed that the additional Pt did not affect the formation of the porous structure. The different color intensities confirm that the prepared particles contained W, O, and Pt elements. The yellow color from the STEM image indicates that Pt metal was well distributed on the prepared particle. We added 0.28 wt % of Pt

DOI: 10.1021/am507935j
ACS Appl. Mater. Interfaces 2015, 7, 3009–3017

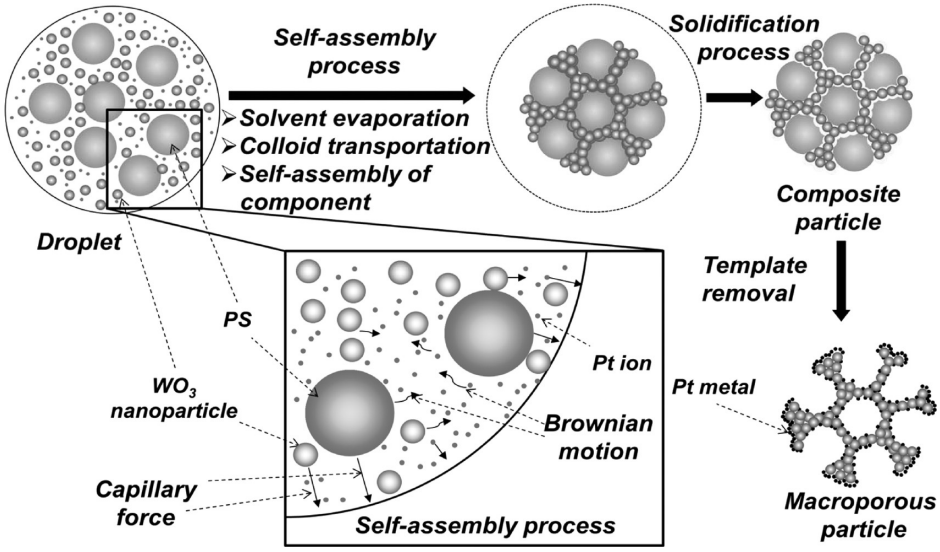

Figure 7. Proposed formation mechanism of the spherical macroporous Pt-modified WO_3 particles.

metal into the initial precursor, which made the final amount of Pt content on the prepared particles 0.23 wt %.

The formation mechanism of the porous WO_3 particles based on the above results is depicted in Figure 7, comprising the following three successive steps: self-assembly, solidification, and template removal.

The self-assembly process occurs at temperatures below 270 °C. This step involves solvent evaporation, colloid transportation, and component self-assembly. Additionally, owing to capillary forces, the smaller components (i.e., WO_3 nanoparticles and Pt ions) move faster to the periphery of the droplet than the larger component (i.e., PS).[26] Solidification between the components was subsequently occurs. Solvent evaporates from the droplet, forming composite particles. Finally, the composite particles are subjected to the template removal process. Based on TG–DTA analysis (Figure 3), all PS components are completely removed by 400 °C, producing macroporous particles as a final product (Figure 4). During the synthesis process, the formation of H_2PtCl_6 $6H_2O$ to Pt metal has following four steps.[27,28] At low temperature, water evaporation occurs and is followed by the decomposition of all Pt solution to $PtCl_4$ at temperature ranging from 150 to 300 °C. When the temperature is between 300 and 500 °C, the $PtCl_4$ starts to decompose and become platinum dichloride ($PtCl_2$). After reaching a temperature of 520 °C, Pt metal is completely formed.[28] This results in the encapsulation of the large components by WO_3, and the Pt components are confirmed by the existence of Pt on the particle surface (Figure 4f).

3.3. Photocatalytic Performance of WO_3 Particles. Figure 8 shows normalized RhB concentrations (with respect to the initial concentration) as a function of time of the photocatalytic experiments conducted under varying WO_3-based catalyst samples. The dotted line represents the blank test (WO_3-free system), whereas the solid line shows the variation in WO_3-based catalysts. As photocatalyst references, we also evaluated the process using WO_3 nanoparticles (open triangle markers) and WO_3 particles prepared from ATP (open circle markers). Unlike the blank test, the RhB concentrations in the presence of all WO_3-based catalysts decreased over time. To evaluate the photocatalytic degradation rate (k), a simplified Langmuir–Hinshelwood kinetics model was used. As observed, the

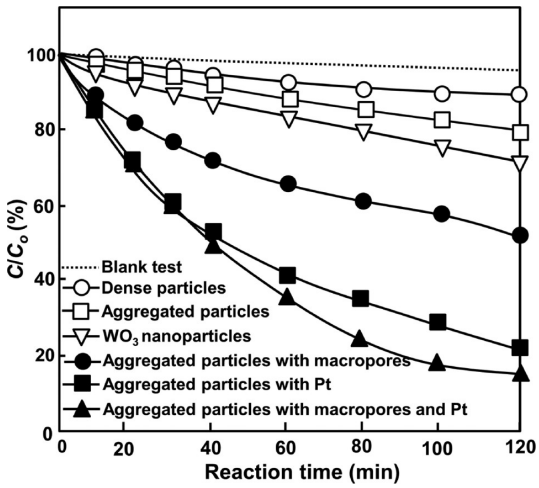

Figure 8. Photodegradation profiles of RhB in the absence of catalyst (dotted line) and the presence of various WO_3-based catalysts.

degradation rate of RhB was dependent on the type of WO_3 catalyst. The lowest photocatalytic rate was obtained using WO_3 catalyst prepared from ATP ($k = 0.966 \times 10^{-3}$ min^{-1}). Changing the WO_3 source from ATP to WO_3 nanoparticles resulted in WO_3 catalyst with a higher catalytic performance (Figure 8, □; $k = 2.352 \times 10^{-3}$ min^{-1}). However, the photocatalytic performance remained is lower than that of WO_3 nanoparticles, in which photocatalytic performance results of WO_3 nanoparticles are shown as open reverse triangles (Figure 8, ▽; $k = 2.976 \times 10^{-3}$ min^{-1}). The presence of additional pores in the particle improved the photocatalytic performance (Figure 8, ●; $k = 6.14.10^{-3}$ min^{-1}), whereby the k value of the macroporous particles is twice that of WO_3 nanoparticles reference.

The presence of Pt co-catalyst considerably improved the photodegradation rate. In the case of the aggregated particles with Pt co-catalyst, the photodegradation rate increases (Figure 8, ■; $k = 13.52 \times 10^{-3}$ min^{-1}). Further, the value of k for aggregated particles is more than 4 times greater than the nanoparticles reference. The combination of the macroporous structure and added Pt in the WO_3-based catalyst resulted in optimum conditions, generating photocatalytic performance

DOI: 10.1021/am507935j
ACS Appl. Mater. Interfaces 2015, 7, 3009–3017

with $k = 17.18 \times 10^{-3}$ min^{-1} (Figure 8, ▲). This result shows that the k value is more than five times higher than that of the nanoparticles reference. The k values obtained for the different WO_3 particles are shown in Table 2.

Table 2. Photodecomposition Rate Constants Determined Experimentally and Surface Area Ratios Calculated Using a Geometric Model

type	WO_3 source	k (10^{-3} min^{-1})[a]	k/k_{ATP}[a]	A/A_{ATP}[b]	A/A_{ATP}[b] BET
dense particles	ATP	0.97	1.00	1.00	1.00
aggregated particles	nanoparticle	2.35	2.43	2.91	7.5
nanoparticle	nanoparticle	2.98	3.08		
aggregated particles with macropores	nanoparticle	6.14	6.35	7.63	27
aggregated particles with Pt	nanoparticle	13.52	13.99	2.91[c]	7.5[c]
aggregated particles with macropores and Pt	nanoparticle	17.18	17.79	7.63[c]	27[c]

[a] k = the photodecomposition rate. [b] A = the surface area of particles. [c] Effect of Pt amount is negligible for the calculating of surface area.

Figure 9 shows the recyclability of aggregated particles with macroporous and additional Pt as a co-catalyst for photo-

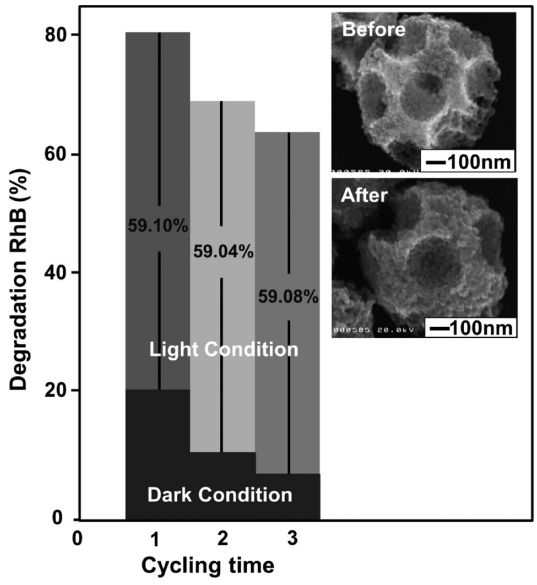

Figure 9. Recyclability performance of aggregated particles with macroporous and Pt addition for photodegradation of RhB.

degradation of RhB, and the inset SEM image shows both before and after three times cycling test, essentially maintain the same morphology. Process degradation of RhB was divided into two zones. First, the process was conducted under dark conditions. Second, the process was conducted under visible light. In general, photocatalytic activity gradually decreased from 80 to 60%. The percentage of degradation RhB in the dark condition decreased from 20 to 6%. However, under visible light, degradation of RhB was almost stable of around 60%. These observations prove that the changes of photocatalytic activity could be associated with the attachment of RhB on the particle surface, resulting in the decreases of absorption capability.

3.4. Correlation between Particle Morphology, Added Pt, and Photocatalytic Activity. On the basis of the photocatalytic results in Figure 8, we concluded different types of WO_3 catalysts produced different photodegradation behaviors of RhB. Considering that all particles featured the same crystal phase (based on XRD analysis in Figure 5), the different photocatalytic behaviors were attributed into two factors: the change in particle morphology and the presence of Pt co-catalyst.

3.4.1. Effect of Particle Morphology. Figure 10 shows the nitrogen adsorption analysis of the prepared particles. The result

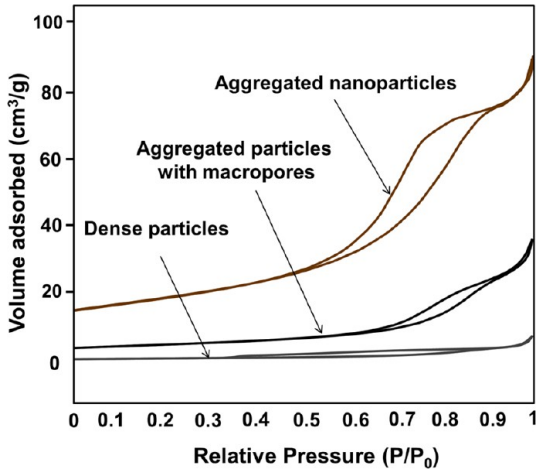

Figure 10. Nitrogen adsorption of the prepared particles.

showed that the prepared particles based on WO_3 nanoparticles with and without additional PS exhibited a characteristic type-IV isotherm, indicating that the prepared particles contained mesoporous structures, while dense particles exhibited characteristic type-II isotherm. The total surface area of aggregated particles was 15 m^2 g^{-1}, that of aggregated particles with macroporous structure was 54 m^2 g^{-1}, and total surface area of dense particles was of 2 m^2 g^{-1}. This proves that aggregated particles have better photocatalytic performance than dense particles due to the existence of mesoporous structure, which can increase the surface area.

Furthermore, in this report, we propose a geometrical analysis model to explain the correlation between particle morphology and surface area (Figure 11). In this model, we focused only on the interaction between the water molecules and surface active catalyst.

When the catalyst is dense with a smooth surface, interactions between the water molecules and surface active sites are limited (Figure 11a). Chemical interactions and light penetration occur only on the particle surface, while the catalytic components inside the catalyst remain inactive.

When the prepared particles are synthesized from WO_3 nanoparticles, the number of surface active sites increases (Figure 11b). The presence of cavities between aggregated nanoparticles promotes the penetration and diffusion of chemical species into the catalyst. Consequently, photocatalytic activity improves. However, owing to the limitation of light penetration into the deepest regions of the catalyst, further catalytic process in the deepest region of catalyst cannot be done well.

To improve further photocatalytic activity, additional presence of a macroporous structure in the catalyst can be used (Figure

DOI: 10.1021/am507935j
ACS Appl. Mater. Interfaces 2015, 7, 3009−3017

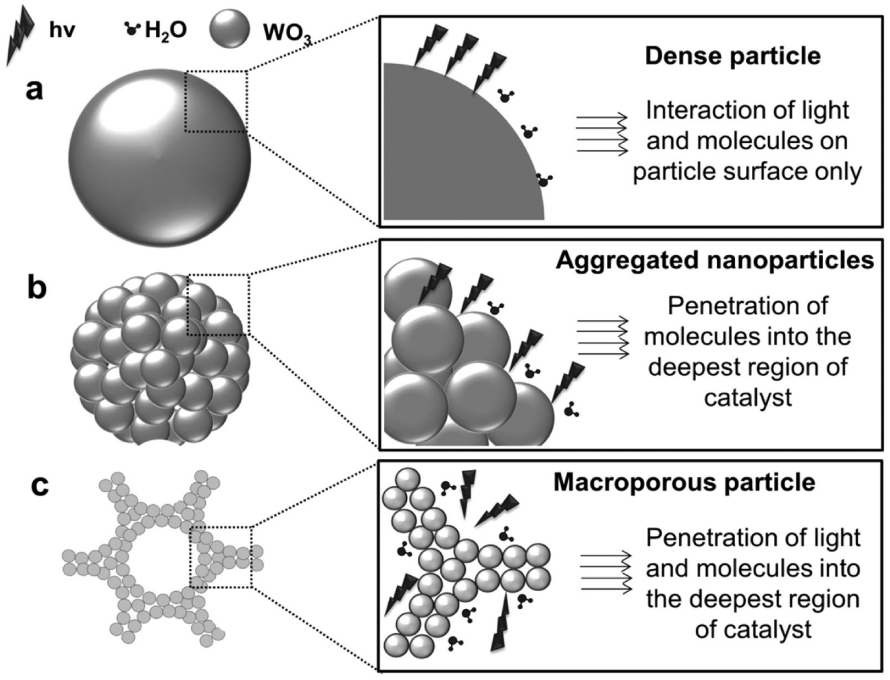

Figure 11. Proposed interaction mechanism between water molecules and surface active sites on WO_3 catalyst with different sizes and structures: (a) dense particles with a smooth surface; (b) aggregated particles (prepared from nanoparticles); and (c) aggregated particles with macropores.

Table 3. Prediction of Surface Area Based on Geometrical Model[a]

Type	Dense particles	Aggregated particles	Aggregated particles with macropores
Model 3D	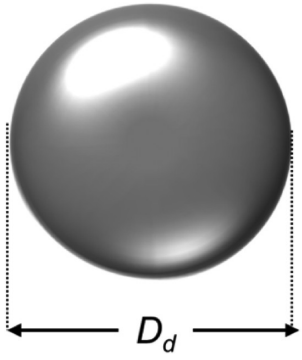	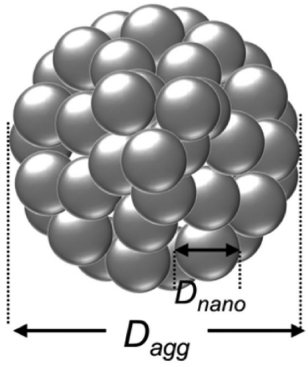	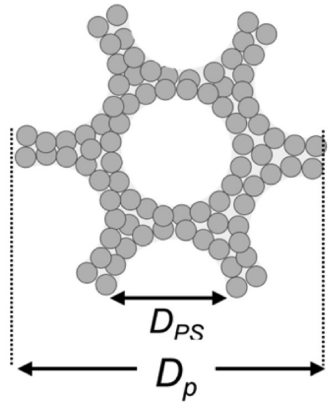
Surface area of a single particle	$A_d = \pi D_d^2$	$A_{agg} = C_D \pi \frac{f}{D_{nano}} \left[D_{agg}^3 - \left(D_{agg} - 2D_{nano} \right)^3 \right]$	$A_{pore}^1 = C_D n_{active} \pi D_{nano}^2 + \pi D_P^2 - \frac{n_{PS} \pi}{8} \left(D_{PS} + 2D_{nano} \right)^2$

[a] A_d = Surface area of a single spherical dense particle; A_{agg} = Surface area of a single spherical particle prepared from aggregated nanoparticles; A^1_{pore} = Surface area of single porous structured particle; D_{PS} = the mean diameter of PS; D_{nano} = the mean diameter of WO_3 nanoparticles; f = the packing fraction; C_D = the number of WO_3 nanoparticles that are active and interact with molecules and light directly; n_{prot} = the number of protruded PS forming holes; n_{active} = the number of active area and interacts with molecules and light

11c). The macropores enable the penetration of both light and chemical species into the deepest region of the catalyst.

A simple geometrical calculation for predicting the surface area as a function of particle morphology is shown in Table 3. We used three types of particle models: dense particles with a smooth surface ("dense particles" model), dense particles prepared from nanoparticles ("aggregated particles" model), and macroporous particles ("aggregated particles with macropores" model). The

DOI: 10.1021/am507935j
ACS Appl. Mater. Interfaces 2015, 7, 3009−3017

ratio of surface area between BET analysis results, and geometrical calculation will be different. To estimate the surface area via a simple geometrical calculation, six assumptions are made: (1) All calculations are based on the same mass of WO_3 used for the photocatalytic process. (2) All particles are homogeneous in size and shape. (3) During the self-assembly process, all components completely fill the space with maximum arrangement. (4) Photon absorption occurs on the particle surface only (Figure SI-1, Supporting Information). (5) No sintering phenomenon between the small aggregated nanoparticles exists. (6) For the aggregated particles with macropores model, all PS components are completely removed; thus, the generated pores are a replication of the PS components in terms of size and shape. Detailed derivations of the equations used in this model are explained in the Supporting Information.

Taking into account the outer diameter of the WO_3 particles of 0.7 μm (based on Ferret analysis of SEM images of the prepared particles), the surface area of aggregated particles model is about 3 times as high as that of dense particles model. Furthermore, the surface area of the aggregated particles with macropores model markedly improved by up to 8 times. On the basis of these results, we can conclude that the change in the morphology directly correlates to the improved photocatalytic performance, which was confirmed by the photocatalytic results displayed in Table 2. Although the trend for the improvement of catalytic activity is proportional to the change of surface area, some errors are found. The experimental results are lower than the calculation of surface area. The dissimilar k value and surface area ratios are because some of catalytic parts do not interact well with both light and chemical species.

3.4.2. Effect of Added Pt. The calculated surface areas of particles in the presence and absence of Pt were similar (Table 2) based on the surface area model in Figure 11. However, the photocatalytic results in Figure 8 showed that the added Pt effectively improved the photocatalytic performance. The k value of the dense particles containing Pt was more than 5 times higher than that without Pt. A higher k value was also observed in the case of aggregated particles with macropores; more specifically, the k value of the aggregated particles with macropores and Pt was almost 3 times as high as that without Pt. These results strongly suggested that loading Pt as a co-catalyst greatly enhanced the photocatalytic performance.

To discuss the effect of Pt co-catalyst on the photocatalytic reaction, we show a mechanism of the photocatalytic process operating in the presence of the Pt-modified WO_3 system in Figure 12. In this model, catalyst activation is possible only upon light irradiation with an appropriate amount of energy. Considering a WO_3 catalyst system, light irradiation ($h\nu$) on the catalyst results in the production of electrons (e^-) in the conduction band (CB) and holes (h^+) in the valence band (VB). These e^- and h^+ are then used for converting oxygen (O_2) and water molecules (H_2O), respectively. However, because WO_3 has a low CB, electron−hole recombination processes occur, consequently leading to reduce production of hydroxyl radicals required for degrading the target organic compound.[29]

In a system containing WO_3 and Pt, an additional reaction mechanism occurs. The work function of WO_3 (5.7 eV) is larger than that of Pt (5.1 eV). When the Pt contacts WO_3, the e^- will migrate from Pt to CB of WO_3 to achieve Fermi level equilibration. Consequently, Pt exhibits an excess positive charge, while WO_3 accumulates excess e^-. Under visible light illumination, Pt acts as an electron pool for trapping the produced e^- as the effect of the deflexed energy band. These are

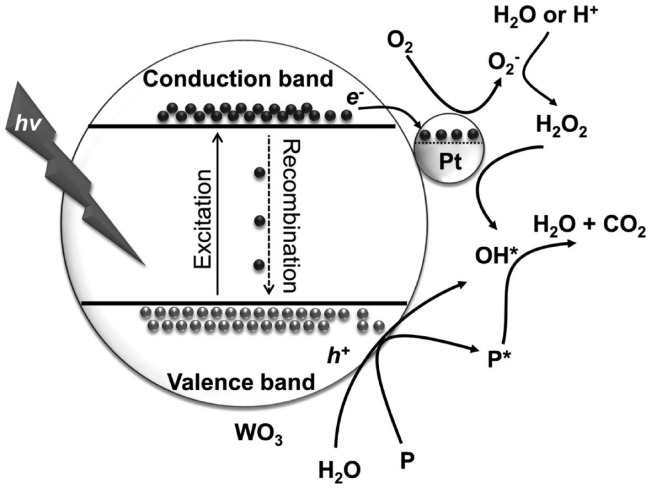

Figure 12. Proposed photocatalysis mechanism operating in the presence of a Pt-modified WO_3 particle system.

trapped to facilitate the multi e^- are then used for further reduction of oxygen molecules, which has more positive potential for $2e^-$ and $4e^-$ than the $1e^-$ reduction. This leads to increased generation of H_2O_2 and then further production hydroxyl radicals (OH*),[9,16,30] as in the following equations:

$$2e^-_{CB} + O_2 + 2H^+ \rightarrow H_2O_2 \quad (1)$$

$$H_2O_2 + e^-_{CB} \rightarrow OH^- + \cdot OH \quad (2)$$

$$h^+_{VB} + H_2O(\text{or } OH^-) \rightarrow \cdot OH \quad (3)$$

Therefore, the small amount of Pt to modified WO_3 catalysts displayed higher photocatalytic performance than bare WO_3, as confirmed in Figure 8.

4. CONCLUSIONS

We successfully synthesized spherical macroporous Pt-modified WO_3 particles using a spray-drying method. The particles were prepared from a precursor containing WO_3 nanoparticles, Pt solution, and PS spheres (as a sacrificial colloidal template). The size and shape of the pores were consistent with that of the initial PS template, suggesting that the pore size of the final product can be regulated accordingly. The number of pores is also controllable by altering the amount of PS added to the precursor. Photocatalytic analysis showed that the changes in particle morphology (from dense with a smooth surface, to dense with a rough surface, to porous structure) and presence of Pt as a co-catalyst effectively improved the photocatalytic activity of WO_3. WO_3 particles prepared at a PS/WO_3 mass ratio of 0.32 and Pt co-catalyst achieved the best photocatalytic results, whereby the photocatalytic rate was more than 5 times higher than that achieved over pure WO_3 nanoparticles. The relationships between the change in particle morphology, added Pt as co-catalyst, and photocatalytic performance were investigated in detail, and corresponding photocatalytic reaction mechanisms were proposed. The current strategy is a gateway toward designing materials with excellent performance but using relatively low amounts of raw materials.

DOI: 10.1021/am507935j
ACS Appl. Mater. Interfaces 2015, 7, 3009−3017

■ ASSOCIATED CONTENT

Supporting Information

Detailed derivation on theoretical calculation of surface area. This material is available free of charge via the Internet at http://pubs.acs.org.

■ AUTHOR INFORMATION

Corresponding Author

* E-mail: ogit@hiroshima-u.ac.jp.

Notes

The authors declare no competing financial interest.

■ ACKNOWLEDGMENTS

We acknowledge support from JSPS KAKENHI (Grant-in-Aid for Young Scientist (A), No. 30508809) and JSPS KAKENHI (Grant-in-Aid for Scientific Research (A), No. 00101197).We thank Dr. Makoto Maeda and Dr. Eishi Tanabe for TEM measurements and discussion. We also thank Shinpei Kaneda for his assistance in this experiment.

■ REFERENCES

(1) de Respinis, M.; De Temmerman, G.; Tanyeli, I.; van de Sanden, M. C.; Doerner, R. P.; Baldwin, M. J.; van de Krol, R. Efficient Plasma Route to Nanostructure Materials: Case Study on the Use of *m*-WO_3 for Solar Water Splitting. *ACS Appl. Mater. Interfaces* **2013**, *5*, 7621−7625.

(2) Deepa, M.; Srivastava, A.; Agnihotry, S. Influence of Annealing on Electrochromic Performance of Template Assisted, Electrochemically Grown, Nanostructured Assembly of Tungsten Oxide. *Acta Mater.* **2006**, *54*, 4583−4595.

(3) Deepa, M.; Srivastava, A.; Lauterbach, S.; Shivaprasad, S.; Sood, K. Electro-optical Response of Tungsten Oxide Thin Film Nanostructures Processed by a Template-Assisted Electrodeposition Route. *Acta Mater.* **2007**, *55*, 6095−6107.

(4) Guo, Y.; Quan, X.; Lu, N.; Zhao, H.; Chen, S. High Photocatalytic Capability of Self-Assembled Nanoporous WO_3 with Preferential Orientation of (002) Planes. *Environ. Sci. Technol.* **2007**, *41*, 4422−4427.

(5) Morales, W.; Cason, M.; Aina, O.; de Tacconi, N. R.; Rajeshwar, K. Combustion Synthesis and Characterization of Nanocrystalline WO_3. *J. Am. Chem. Soc.* **2008**, *130*, 6318−6319.

(6) Jiao, Z.; Wang, J.; Ke, L.; Sun, X. W.; Demir, H. V. Morphology-Tailored Synthesis of Tungsten Trioxide (Hydrate) Thin Films and Their Photocatalytic Properties. *ACS Appl. Mater. Interfaces* **2011**, *3*, 229−236.

(7) Zoontjes, M. G.; Huijben, M.; Baltrusaitis, J.; van der Wiel, W. G.; Mul, G. Selective Hydrothermal Method to Create Patterned and Photoelectrochemically Effective Pt/WO_3 Interfaces. *ACS Appl. Mater. Interfaces* **2013**, *5*, 13050−13054.

(8) Ng, C.; Ng, Y. H.; Iwase, A.; Amal, R. Influence of Annealing Temperature of WO_3 in Photoelectrochemical Conversion and Energy Storage for Water Splitting. *ACS Appl. Mater. Interfaces* **2013**, *5*, 5269−5275.

(9) Kim, J.; Lee, C. W.; Choi, W. Platinized WO_3 as an Environmental Photocatalyst that Generates OH Radicals under Visible Light. *Environ. Sci. Technol.* **2010**, *44*, 6849−6854.

(10) Huang, H.; Yue, Z.; Song, Y.; Du, Y.; Yang, P. Mesoporous Tungsten Oxides as Photocatalysts for O_2 Evolution under Irradiation of Visible Light. *Mater. Lett.* **2012**, *88*, 57−60.

(11) Ashkarran, A.; Ahadian, M.; Ardakani, S. M. Synthesis and Photocatalytic Activity of WO_3 Nanoparticles Prepared by the Arc Discharge Method in Deionized Water. *Nanotechnology* **2008**, *19*, 195709.

(12) Martínez-de la Cruz, A.; Martínez, D. S.; Cuéllar, E. L. Synthesis and Characterization of WO_3 Nanoparticles Prepared by the Precipitation Method: Evaluation of Photocatalytic Activity under Vis-Irradiation. *Solid State Sci.* **2010**, *12*, 88−94.

(13) Xu, Z.; Tabata, I.; Hirogaki, K.; Hisada, K.; Wang, T.; Wang, S.; Hori, T. Preparation of Platinum-Loaded Cubic Tungsten Oxide: A Highly Efficient Visible Light-Driven Photocatalyst. *Mater. Lett.* **2011**, *65*, 1252−1256.

(14) Elezovic, N.; Babic, B.; Ercius, P.; Radmilovic, V.; Vracar, L. M.; Krstajic, N. Synthesis and Characterization Pt Nanocatalysts on Tungsten Based Supports for Oxygen Reduction Reaction. *Appl. Catal. B* **2012**, *125*, 390−397.

(15) Luo, J. Y.; Gong, L.; Tan, H. D.; Deng, S. Z.; Xu, N. S.; Zeng, Q. G.; Wang, Y. Study of the Catalyst Poisoning and Reactivation of Pt Nanoparticles on the Surface of WO_3 Nanowire in Gasochromic Coloration. *Sensors and Actuat. B* **2012**, *171*, 1117−1124.

(16) Miyauchi, M. Photocatalysis and Photoinduced Hydrophilicity of WO_3 Thin Films with Underlying Pt Nanoparticles. *Phys. Chem. Chem. Phys.* **2008**, *10*, 6258−6265.

(17) Shiraishi, Y.; Sugano, Y.; Ichikawa, S.; Hirai, T. Visible Light-Induced Partial Oxidation of Cyclohexane on WO_3 Loaded with Pt Nanoparticles. *Catal. Sci. Technol.* **2012**, *2*, 400−405.

(18) Cui, X.; Shi, J.; Chen, H.; Zhang, L.; Guo, L.; Gao, J.; Li, J. Platinum/Mesoporous WO_3 as a Carbon-free Electrocatalyst with Enhanced Electrochemical Activity for Methanol Oxidation. *J. Phys. Chem. B* **2008**, *112*, 12024−12031.

(19) Yan, Z.; Wei, W.; Xie, J.; Meng, S.; Lü, X.; Zhu, J. An Ion Exchange Route to Produce WO_3 Nanobars as Pt Electrocatalyst Promoter for Oxygen Reduction Reaction. *J. Power Sources* **2013**, *222*, 218−224.

(20) Nandiyanto, A. B. D.; Arutanti, O.; Ogi, T.; Iskandar, F.; Kim, T. O.; Okuyama, K. Synthesis of Spherical Macroporous WO_3 Particles and their High Photocatalytic Performance. *Chem. Eng. Sci.* **2013**, *101*, 523−532.

(21) Arutanti, O.; Ogi, T.; Nandiyanto, A. B. D.; Iskandar, F.; Okuyama, K. Controllable Crystallite and Particle Sizes of WO_3 Particles Prepared by a Spray-Pyrolysis Method and Their Photocatalytic Activity. *AIChE J.* **2014**, *60*, 41−49.

(22) Arutanti, O.; Nandiyanto, A. B. D.; Ogi, T.; Iskandar, F.; Kim, T. O.; Okuyama, K. Synthesis of Composite WO_3/TiO_2 Nanoparticles by Flame-Assisted Spray Pyrolysis and Their Photocatalytic Activity. *J. Alloys Compd.* **2014**, *591*, 121−126.

(23) Purwanto, A.; Widiyandari, H.; Ogi, T.; Okuyama, K. Role of Particle Size for Platinum-Loaded Tungsten Oxide Nanoparticles during Dye Photodegradation under Solar-Simulated Irradiation. *Catal. Commun.* **2011**, *12*, 525−529.

(24) Ogi, T.; Nandiyanto, A. B. D.; Okuyama, K. Nanostructuring Strategies in Functional Fine-Particle Synthesis towards Resource and Energy Saving Applications. *Adv. Powder Technol.* **2014**, *25*, 3−17.

(25) Nandiyanto, A. B. D.; Suhendi, A.; Ogi, T.; Iwaki, T.; Okuyama, K. Synthesis of Additive-free Cationic Polystyrene Particles with Controllable Size for Hollow Template Applications. *Colloids Surfaces A* **2012**, *396*, 96−105.

(26) Nandiyanto, A. B. D.; Okuyama, K. Progress in Developing Spray-Drying Methods for the Production of Controlled Morphology Particles: From the Nanometer to Submicrometer Size Ranges. *Adv. Powder Technol.* **2011**, *22*, 1−19.

(27) Li, N.; Hu, Z.; Zheng, M.; Lu, H.; Zhao, B.; Zhang, S.; Zheng, J.; Ji, G.; Cao, J. Formation of Pt Nanoparticles in Mesoporous Silica Channels via Direct Low-Temperature Decomposition of $H_2PtCl_6 \cdot 6H_2O$. *Mater. Lett.* **2013**, *106*, 193−196.

(28) Hernandez, J. O.; Choren, E. A. Thermal Stability of some Platinum Complexes. *Thermochim. Acta* **1983**, *71* (3), 265−272.

(29) Wen, Z.; Wu, W.; Liu, Z.; Zhang, H.; Li, J.; Chen, J. Ultrahigh-Efficiency Photocatalysts based on Mesoporous Pt−WO_3 Nanohybrids. *Phys. Chem. Chem. Phys.* **2013**, *15*, 6773−6778.

(30) Yang, F.; Takahashi, Y.; Sakai, N.; Tatsuma, T. Photocatalytic Remote Oxidation Induced by Visible Light. *J. Phys. Chem. C* **2011**, *115*, 18270−18274.

DOI: 10.1021/am507935j
ACS Appl. Mater. Interfaces 2015, 7, 3009−3017